Synthesis of SnO_2/RGO nanocomposite and its superior capacitive performance as supercapacitor electrode materials

WEIDONG CHEN[a], ZHONGAI HU[b], YANLI CHEN[*,a]
[a]*Gansu Vocation Technical College of Nonferrous Metallurgy, Jinchang 737100, Gansu, China*
[b]*Key Laboratory of Eco-Environment-Related Polymer Materials of Ministry of Education, Key Laboratory of Polymer Materials of Gansu Province, College of Chemistry and Chemical Engineering, Northwest Normal University, Lanzhou 730070, PR China*

SnO_2 nanoparticles supported by reduced graphene oxide (SnO_2/RGO composites) have been fabricated through a simple chemical route in a water system. Field emission scanning electron microscopy (FESEM) and transmission electron microscopy (TEM) observation of the composite with mass ratio of 76.1:23.9 (SnO_2:RGO) reveals that SnO_2 nanoparticles (about 4-8 nm in size) locate on RGO sheets homogeneously. Interestingly, the morphology features of RGO in composites are influenced by the number of loaded SnO_2 nanoparticles. In the composite, SnO_2 act as spacers to prevent effectively the agglomeration of RGO sheets while the RGO sheets in good dispersion server as a conductor for fast electron transfer between the active materials and charge collector, as well as buffered spaces to accommodate the volume expansion/contraction during discharge/charge process. The composite, as electrode materials in supercapacitors, exhibited a specific capacitance as high as 326 F/g at the specific current of 1 A/g in 1M H_2SO_4 electrolyte in the potential window from 0 to 1.0 V. Furthermore, the composite was testified to have rather excellent cycle life along with about 97.2% specific capacitance retained after 1000 cycle tests. These results indicate that the electrochemical capacitive performance of as-prepared nanocomposites could be enhanced by the positive synergistic effect between RGO and SnO_2.

(Received March 4, 2017; accepted April 5, 2018)

Keywords: Tin oxide, Reduced graphene oxide, Composites, Enhanced electrochemical capacitance

1. Introduction

Pseudocapacitor (also known as electrochemical capacitor) is a unique electrochemical device, which is designed to possess high specific energy, long cycle life and high cycle efficiency. Such advantageous characteristics of pseudocapacitors render them very suitable as auxiliary power sources for electric vehicles and plug-in electric vehicles. Generally, on the basis of the energy storage mechanism, supercapacitors establish capacitance via two ways, electric double layer (EDL) effects and pseudocapacitance [1]. For EDL capacitors, carbon-based materials with a high surface area are commonly used, and the capacitance comes from the charge accumulated at the electrode/electrolyte interface. On the other hand, the pseudocapacitors or redox supercapacitors use conducting polymers and metal oxides as electrode materials, which undergo fast and reversible faradic redox reaction. It is recognized that RuO_2 and IrO_2 are typical pseudocapacitive electrode materials with remarkable performance [2-5]. However, the application potential of these materials has been hindered by their relatively high costs. Alternative materials, such as nickel oxide [6], cobalt oxide [7], manganese oxide [8,9], vanadium oxide [10], zinc oxide [11] and tin oxide [12,13] were paid to increasing attention. Among these materials, SnO_2 presents high concentration because of its low cost and environmentally benign nature. Sb-doped SnO_2 nanocrystallite thin film synthesized by solegel process was reported to show a specific capacitance value of 16 F g^{-1} [14]. Besides, amorphous nanostructured tin oxide was potentiodynamically deposited onto stainless steel (SS) electrode [15], and the specific capacitance (SC) of 285 F g^{-1} was obtained from CV at a scan rate of 10 mV s^{-1}. In the practical processes, SnO_2 did not seem to show excellent capacitive behaviors although it had relatively high conductivity and varying solid-state redox couples. Therefore, researchers have been seeking the effective strategies to improve the specific capacitance of SnO_2 by reducing its grain size and constructing the microstructure with large specific area as well as preparing composites. Recently, SnO_2 has been used as guest material to be loaded on the carbonaceous nanostructures to achieve the improvement in the electrochemical performance [16,17].

Graphene is an excellent substrate to host active nanomaterials for energy applications due to its high conductivity, large surface area, flexibility, chemical stability, and low manufacturing cost. Growing nanomaterials with well-defined morphology on highly pristine and electrically conducting graphene remains a major topic of interest. The advantages of graphene-based nanocomposite materials can be found in two aspects: On one hand, the loading of electrochemical active species can avoid or decrease the possibility of serious agglomeration or restacking of graphene sheets ensembles, and consequently provide a higher available

electrochemically active surface area for increasing electric double layer capacitance energy storage, owing to the spacing effect of loaded particles between neighboring. On the other hand, the electrochemical active species sit on graphene sheet can contribute supercapacitance through fast Faraday reaction. Recent works have shown the potential applications of oxides/hydroxides [18–23] coupled with graphene sheets in supercapacitors. However, the CV curves of such materials often display obvious redox peaks and the corresponding constant current discharge curves are not linear. In this case, electrochemical process is generally in concomitance with polarizations which deteriorate rate capability and cycle life, especially at a large current density. Athough the CV curves of the composites composed of SnO_2 and graghene show a idea capacitive features, a maximum specific capacitance has been reported to be only as high as 42.7 F/g. [24–26] As a result, the positive synergistic effect of the composites is not brought into play due to serious aggregation of graphene nanosheets or inefficient active utilization of SnO_2. Therefore, seeking effective strategies to synthesize well-dispersed composites to present the excellent capacitive performances of the materials is quite important.

Delamination of layered graphite oxide (GO) in solvents under suitable conditions results in colloidal dispersions of solvated, two dimensional nanosheets. Basal planes of those nanosheets are decorated mostly with epoxy and hydroxyl groups, while carbonyl and carboxyl groups located at the edges. These oxygenated functional groups can act as nucleation centers to anchor active materials onto grapheme oxide sheets. Hence, it could be feasible to synthesize well-dispersed graphene-based composites directly starting with GO. To implement this object, we have developed an adoptable two-step method to improve the specific capacitance through integrating metal oxide particles together with RGO to form hybrid nanostructured composites. In our early work, ZnO/RGO composites had been synthesized through this method, in which the pseudocapacitance contributed by zinc oxide nanoparticles incorporated with the electrical double layer capacitance rising from reduce grapheme oxide, thus improving the electrochemical performance in terms of specific capacitance and power density [27]. In the present work, we demonstrated that the two-step method was also available for preparing SnO_2/RGO composites. A homogeneous dispersion of reduced graphene oxide (RGO) and SnO_2 nanoparticles in the composite were achieved, and an extraordinary high specific capacitance was obtained. Moreover, the composite exhibited a high power density and reasonable cycling performance, indicating that the SnO_2/RGO composites could be a promising supercapacitor electrode material.

2. Experimental section

2.1. Preparation of GO

Reagents were all of AR grade. Water used in the synthesis and washing was deionized. Graphite oxide was prepared from natural graphite powder by a modification of Hummers method [28]. One gram of graphite powder was added to 23 mL of cooled (0 °C) concentrated H_2SO_4. Three grams of $KMnO_4$ was added gradually with stirring and cooling, so that the temperature of the mixture was maintained below 20 °C. The mixture was then stirred at 35 °C for 30 min. 46 mL of distilled water was slowly added to cause an increase in temperature to 98 °C, and the mixture was maintained at this temperature for 15 min. The reaction was terminated by adding 140 mL of distilled water followed by 10 mL of 30% H_2O_2 solution. The solid product was separated by centrifugation, washed repeatedly with 5% HCl solution until sulfate could not be detected by $BaCl_2$, and then washed 3-4 times with ethanol and dried in vacuum at 60°C overnight.

2.2. Synthesis of composites

The SnO_2/RGO composites with different mass ratios were synthesized through a two-step method. The typical route is as follows: In the first step, $SnCl_4 \cdot 5H_2O$ (0.8765 g) was dissolved in distilled water (25 ml) with vigorous stirring in an ice-bath. Then, GO (0.2090 g) was exfoliated in distilled water (125 ml) with ultrasonic treatment for an hour to form a light-brown solution. Subsequently, the above GO solution was dropped into aqueous solution with continuous stirring. Afterwards, $NH_3 \cdot H_2O$ (12—15%) was dropwise added into the above mixture until the pH up to 8.5. After aging for 12 h, the product was dried at 60 °C. Through those procedures, the precursor composites were obtained. In the second step, the precursors were heated at 200 °C for 5 h in air with a rate of 5 °C min^{-1} in muffle stove. The product rinsed with distilled water several times, and then dried at 60 °C for 12 h under vacuum. The various amount of reactants results in the composites with different mass ratios. For comparison, SnO_2 was prepared by the same procedure in the absence of GO.

2.3. Characterization

Powder X-ray diffraction (XRD) of samples was performed on a diffractometer (D/Max-2400) with Cu Kα radiation (λ=1.5418 Å) at 40 kV, 60 mA. The morphology was observed with field emission scanning electron microscopy (FESEM) (JSM-6701F, Japan) and transmission electron microscopy (TEM) (JEOL, JEM-2010, Japan). Raman spectra were recorded with a Raman Station BRUKER (RFS 100/S) using a near infrared laser operating at 1064 nm with a CCD detector. Thermogravimetric (TG) analysis was carried out using a Perkin-Elmer TG/DTG–6300 instrument in a temperature range of 30–750 °C. A heating rate of 10 °C min^{-1} in air with a flow rate of 20 mL min^{-1} was used.

2.4. Preparation of working electrode

The working electrodes were prepared by mixing active materials with 10 wt.% acetylene black, 10 wt.% conducting graphite and 5 wt.% polytetrafluoroethylene (PTFE). A small amount of ethanol was dropwise added into the above mixture to form slurry by sonicating. The slurry was pressed on a graphite current collector. Each working electrode contained about 1 mg of electroactive material and had a geometric surface area of about 1 cm^2. The as-prepared electrode was dried at room temperature for 24 h.

2.5. Electrochemical tests

A typical three-electrode experimental cell equipped with a working electrode, a platinum foil counter electrode, and Ag/AgCl reference electrode was used for measuring the electrochemical properties of working electrode. All electrochemical measurements were carried out in 1 M H_2SO_4 solution as electrolyte. Cyclic voltammetry (CV), galvanostatic charge-discharge and electrochemical impedance spectroscopy (EIS) were carried out on the CHI660B electrochemical working station.

3. Results and discussion

3.1. TG analysis of composites

TG analyses were carried out to determine the chemical composition of as-prepared SnO_2/RGO composites. Fig. 1 shows the TG curves of the composites with different mass ratio. Generally, some vacancies and topological defects can be simultaneously produced on the graphene sheets due to the release of carbon dioxide during the thermal expansion. These defect sites lead to a decrease of the thermal stability of these composites at elevated temperature [29]. As shown in Fig. 1, two steps appear for mass loss of all the samples. Taking the composite with mass ratio of 76.1:23.9 (SnO_2:RGO) as an example, the TG curve shows an initial weight loss of 3.5 wt% at around 122 °C, which is due to the desorption of physically absorbed water. The main weight loss of 23.9 wt% occurs at the temperature range of 400–680 °C, which may be caused by the removal of RGO from the composite. In this temperature range, the weight percent of the sample drops from 96.8 to 72.9 wt%. Thus the sample contains approximately 23.9 wt% of RGO. After 680 °C, the TG traces are stable with no further weight loss, which means a complete removal of RGO. The estimations of other composites based on the TG curves indicate that the SnO_2/RGO mass ratios of samples are 82:18, 78.4:21.6, 73.8:26.2, 71.2:28.8 and 68.5:31.5, respectively.

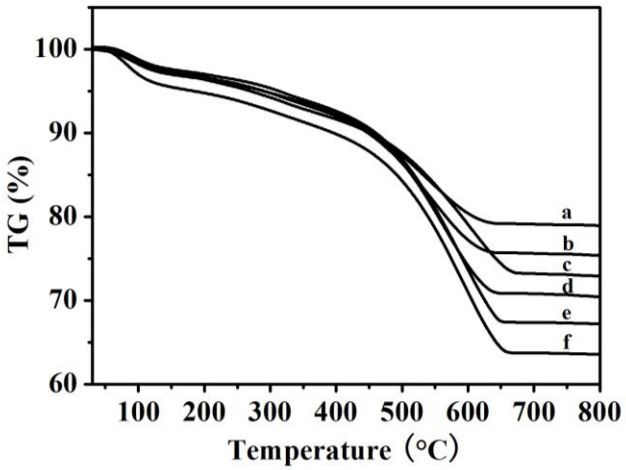

Fig. 1. TG curves of as-prepared SnO_2/RGO composites with mass ratios of SnO_2 to RGO up to 82:18 (a), 78.4:21.6 (b), 76.1:23.9(c), 73.8:26.2 (d), 71.2:28.8 (e) and 68.5:31.5 (f) under air atmosphere

3.2. Morphology features of composites

The surface morphologies of the as-synthesized composite with the mass ratio of 76.1:23.9 (SnO_2:RGO) are imaged by FESEM, as shown in Fig. 2 (a, b). In low magnification, a gigantic sheet can be observed. The further observation demonstrates that the surface of the sheets is corrugated or curly (Fig. 2a). It has been reported that the corrugation and scrolling are part of the intrinsic nature of RGO, which result from a fact that the 2D membrane structure tends to become thermodynamically stable via bending [30]. The FESEM image in high magnification shows a unique feature that a great amount of SnO_2 particles have spread on the RGO sheets with tight interaction (Fig. 2b). For comparison, the FESEM images of pure SnO_2 shown in Fig. 2 (c, d) display clearly that the blocks of SnO_2 particles are formed in different sizes, typically in low magnification. Besides, in high magnification, as shown in Fig. 2 (d), the size of SnO_2 particles is larger than that of well-dispersed on RGO sheets in composite. These results indicate that the existence of RGO could both reduce the agglomeration and the size of SnO_2 particles effectively.

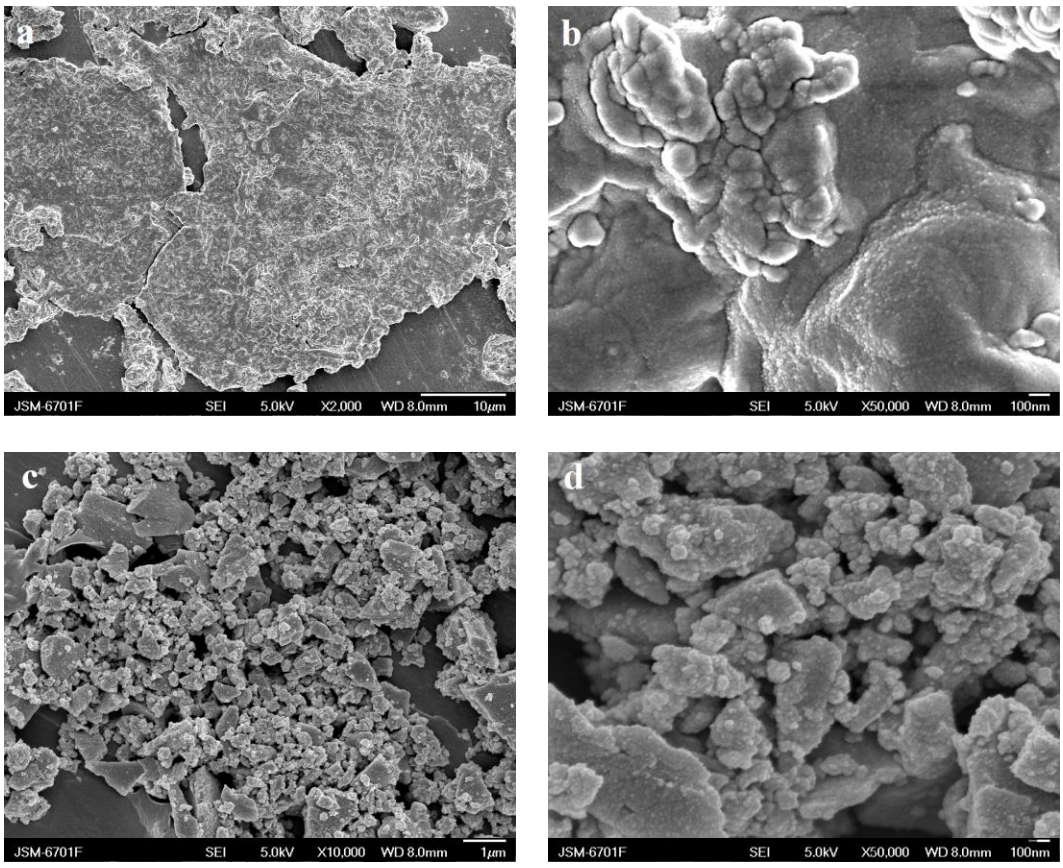

Fig. 2. FESEM images of SnO_2/RGO composite with mass ratios of SnO_2 to RGO up to 76.1:23.9 (a, b) and pure SnO_2 (c, d)

To analyze detailed morphology feature of SnO_2 particles grown on the RGO sheets, we take the composite with the mass ratio of 76.1:23.9 (SnO_2:RGO) as an example to carry out TEM observation (Fig. 3). It is identified from the image in Fig. 3a that a great amount of SnO_2 nanoparticles with small size were uniformly distributed on the surface of graphene nanosheets. TEM observation at a higher magnification (the insert in Fig. 3a) even more demonstrates that the SnO_2 nanoparticles on the RGO sheets construct as a porous structure, in which the pores distribute homogeneously through the arrays of SnO_2 nanoparticles on the RGO sheets. This unique structure can not only allow the penetration of the electrolyte ion in the outer region of the solids but also in the inner region, which increases the liquid–solid interfacial area, provides a path for the insertion and extraction of ions, and ensures a high reaction rate. Interestingly, the morphologies of graphene in composites are influenced differently by the number density of SnO_2 nanoparticles which attached on the RGO sheets. When an amount of SnO_2 nanoparticles are grown on the RGO sheets sparsely, the scrolling nature of RGO sheet is mainly revealed (Fig. 3b and c), even some sheets agglomerated together to form cluster (Fig. 3d). In addition, the TEM image in higher magnification (insert in Fig. 3b) shows that the SnO_2 nanoparticles on graphene nanosheets are quite uniform, with a size range of 4-8nm. Oppositely, as the number density of SnO_2 nanoparticles increased, which is shown in Fig. 3e, the corrugated and curly characteristic of graphene becomes weak correspondingly due to surface interaction between SnO_2 particles and RGO sheets. Furthermore, from Fig. 3f, it can be observed that the RGO sheets coated by SnO_2 particles are disordered stacking, indicating that the SnO_2 nanoparticles on the surface of graphene sheets also acting as spacers efficiently preventing the closely restacking of graphene sheets, which avoids the loss of their high active surface. Summarized the results from SEM and TEM, it is believable that the interaction between SnO_2 particles and RGO sheets influence each of them positively. On one hand, more small-sized and more uniform SnO_2 particles could be achieved on the surface of RGO sheets. On the other hand, closely restacking of graphene sheets is reduced by SnO_2 particles which act as spacers. Hence, under an optimal mass ratio, well-dispersed SnO_2/RGO composites with more active surface are synthesized.

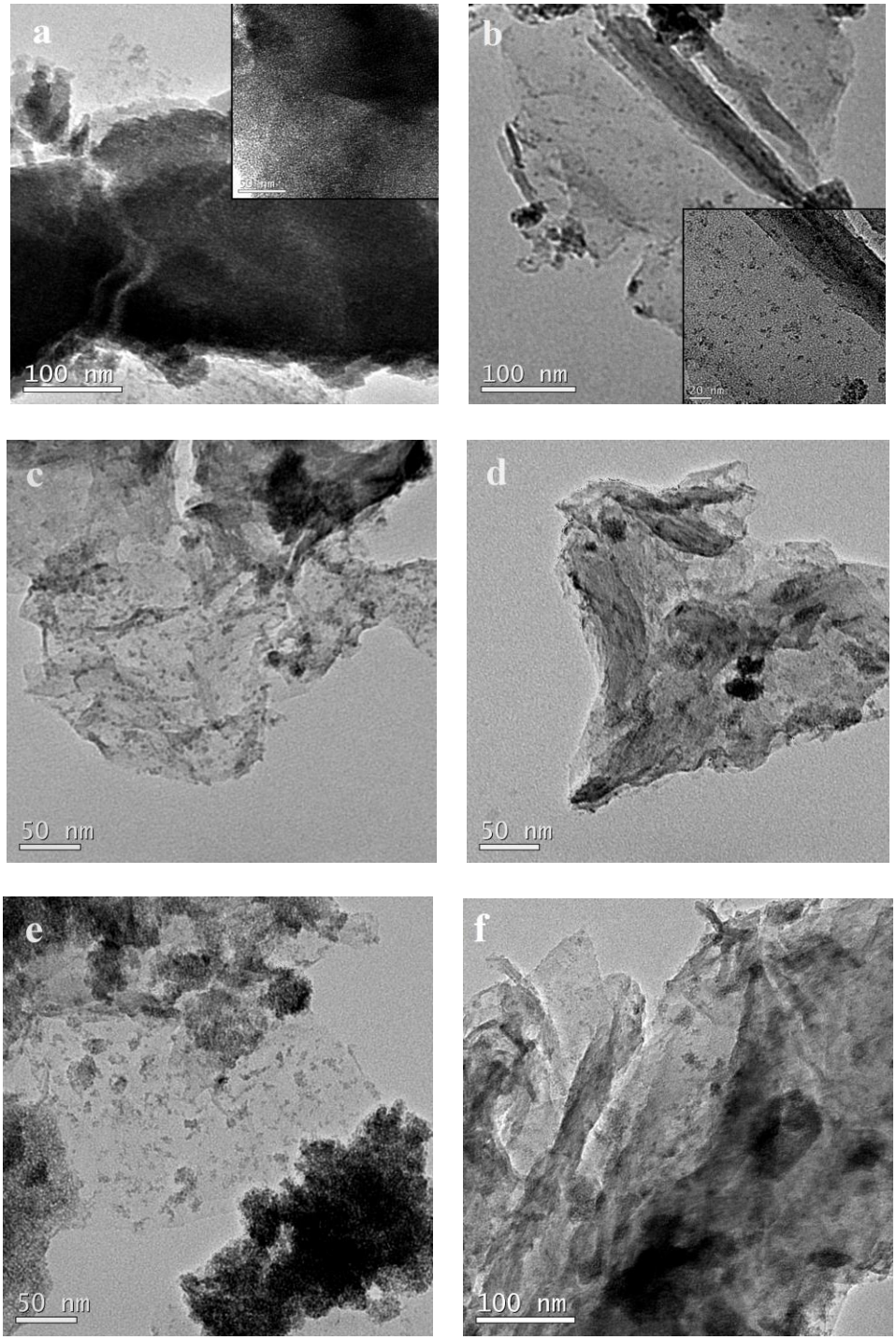

Fig. 3. TEM images of SnO_2/RGO composite with mass ratios of SnO_2 to RGO up to 76.1:23.9 (a, b, c, d, e, f)

3.3. Formation processes of composites

To interpret those observed results of SEM and TEM images, the formation process of SnO_2/RGO composites is speculated. As reported by previous studies, GO sheets have their basal planes decorated mostly with epoxy and hydroxyl groups, while carbonyl and carboxyl groups are located at the edges [31]. These groups enable the subsequent formation of nanostructures which could attach on the surfaces and edges of GO sheets. At the initial stage of the reaction, Sn^{4+} ions, formed by the dissolution of $SnCl_4$ in deionized water, favorably bind with the O atoms of the negatively charged oxygen-containing functional groups on GO sheets through an electrostatic force or ion-exchange with H^+ from carboxyl. Usually, there are two interactions between GO sheets, electrostatic

interaction and van der Waals interaction. If the electrostatic repulsion is dominant, graphene oxides could well disperse in the reaction systems. On the contrary, if the van der Waals interaction dominates, the irreversible coagulation of the exfoliated RGO occurs during the reaction process. Consequently, when tin ions and GO is up to a proper mass ratio, well-dispersed colloids of graphite oxide sheets might be formed. With the addition of $NH_3 \cdot H_2O$ solution, a large number of nuclei on the GO sheets were formed in a short time. These nuclei interrupt the agglomeration of GO sheets, and provide the probability to form homogeneous dispersion of SnO_2 particles on GO sheets. At the second stage of the reaction, annealing was carried out to convert GO sheets into RGO sheets, and the attached SnO_2 particles on the GO sheets effectively prevents the agglomeration of the graphene sheets during the annealing process. After thermal treatment, the formed SnO_2 particles can serve as spacers to prevent aggregation of individual graphene sheets, and form a particle–sheet structured SnO_2/RGO composite. It is reasonable to expect that such composites have a rich porous structure and large available surface area for the charge-storage/delivery process.

3.4. Phase state of samples

The crystal phase and structure information of the products were obtained by XRD measurements. The XRD patterns of GO, RGO extracted from composites and SnO_2/RGO composites are shown in Fig. 4. As shown in Fig. 4(1), graphite oxide has a dominant peak centered at 2θ value of 10.3°, corresponding to the (001) inter-planar spacing of 8.3 Å and it matches well with the values reported in the literature [32]. In XRD patterns of RGO extracted from the composite, the (001) peak of GO was disappeared. Two characteristic reflection peaks of graphene appear at 2θ values of 24.8° and 45°, indicating that most of GO nanosheets are reduced into RGO after the thermal treatment. The low broad (002) diffraction peak appears at 2θ =24.8°, showing the disorderedly stacked RGO sheets. This broad peak is weaker than that of graphene film [33], which obtained by filtrating aqueous dispersion of GO and then reducing by thermal treatment, suggesting less agglomeration and more disordered stacking for RGO sheets in comparison with graphite. The X-ray diffraction patterns of the SnO_2/RGO composites in Fig. 4(2) comprise five peaks appearing at 2θ values of 26.5°, 33.7°, 37.2°, 51.9° and 65.4°, corresponding to the crystal planes of (110), (101), (200), (211) and (301), respectively. The five peaks can be indexed to the tetragonal rutile SnO_2 phase, which are consistent with the values in the standard card (JCPDS No. 41-1445). Additionally, no impurity peaks were observed in all the curves, which indicated that high-purity SnO_2 was synthesized in the SnO_2/RGO composites. The crystallite domain size calculation was performed basing on the major diffraction peak (110) by using the Scherrer's formula ($D=0.89\lambda/B\cos\theta$), where λ, B and θ are the wavelength of X-ray (1.5418 Å) for $CuK\alpha_1$ radiation, full width at half maximum and peak position, respectively. The estimated grain size was calculated to be about 7 nm which is in good agreement with TEM observation. Moreover, the diffraction peaks (curve c) of the composite with the mass ratio up to 76.1:23.9 (SnO_2:RGO) are weaker than that of others. The RGO sheets coated by SnO_2 are in a state with more disordered stacking at this ratio and SnO_2 has a relative small crystalline size.

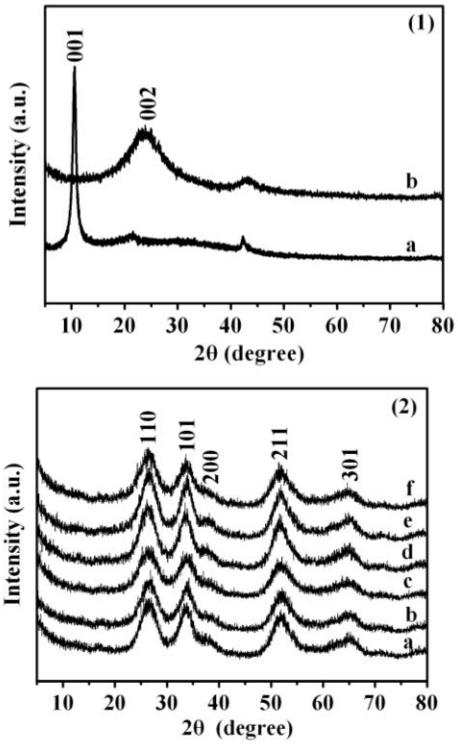

Fig. 4. XRD patterns of samples: (1) GO (a) and RGO extracted from the composite (b); (2) the SnO_2/RGO composite with different mass ratios of SnO_2 to RGO up to 82:18 (a), 78.4:21.6 (b), 76.1:23.9(c), 73.8:26.2 (d), 71.2:28.8 (e) and 68.5:31.5 (f)

3.5. Raman spectrum

Raman spectroscopy is a powerful nondestructive tool to characterize carbonaceous materials. Fig. 5 shows a typical spectrum of the composite with the mass ratio of 76.1:23.9 (SnO_2:RGO) over the measured spectral range. According to the group theory, SnO_2 has the tetragonal rutile structure (space group D_{4h}^{14}, $P4/mnm$) with two SnO_2 molecules per unit cell. The irreducible representations of the optic modes are $\Gamma = \Gamma_1^+(A_{1g})+\Gamma_2^+(A_{2g})+\Gamma_3^+(B_{1g})+\Gamma_4^+(B_{2g})+\Gamma_5^-(E_g)+\Gamma_1^-(A_{2u})+2\Gamma_4^-(B_{1u})+3\Gamma_5^+(E_u)$, where five modes of A_{1g}, B_{1g}, B_{2g} and E_g are Raman active, seven modes of A_{2u} and $3E_u$ are IR active and two modes of A_{2g} and B_{1u} are inactive [34,35]. Two fundamental Raman peaks at 479 and 774 cm^{-1}, corresponding to the E_g and B_{2g} vibration modes, respectively [36]. The band at 309 cm^{-1} can be indexed to IR-active $E_u(3)$ TO mode (TO is the mode of the transverse optical phonons). All these Raman features confirm that the as-synthesized SnO_2 in composite possess the characteristics of the tetragonal rutile structure. This

result agrees with the XRD studies. Moreover, the Raman line at 514 cm^{-1} was observed, which could not be observed in SnO_2 bulk [37]. This peak is close to the IR-actived A_{2u} mode at 512 cm^{-1} for TO, calculated theoretically. In the nanosized crystal, some IR active modes will lose their IR activity and become Raman active with decreasing size and increasing disorder [38]. This can explain the appearance of the peak at 514 cm^{-1}. The band centered at 574 cm^{-1} was reported for SnO_2 nanoparticles, which was ascribed to amorphous hydrous tin (IV) oxide [39]. In the radiative transition process of the SnO_2 1D nanostructure, the photoinduced excitons can propagate along the longitudinal axis with long length. It certainly produces enhanced coupling between exciton and phonon via Fro¨hlich long-range interaction. This coupling can induce a multiphonon transition via the local deformation. So the resonant enhanced modes of 971 (E_g+E_g) and 1113 cm^{-1} (E_g+A_{1g}) are necessarily observed for their overlap to lead to a giant oscillator strength and emit collectively because the 1D structure is a natural Fabry-Perot cavity [40]. In addition, raman peaks of graphene (D line and G line) can be well distinguished. The band at 1587 cm^{-1} was assigned to the G band, which is usually assigned to the E_{2g} phonon of C sp^2 atoms, while the D line is a breathing mode of κ-point phonons of A_{1g} symmetry [41]. It is worth noting that both the characteristic peaks of the RGO and of SnO_2 are observed in SnO_2/RGO composite, indicating that the composite is composed of SnO_2 and RGO.

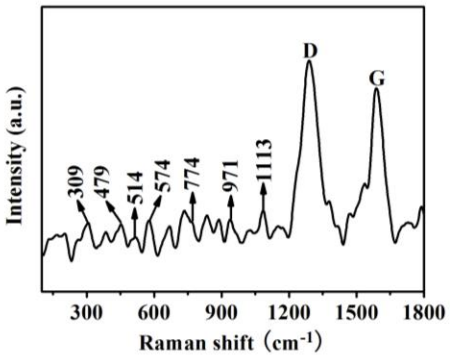

Fig. 5. Raman spectrum of SnO_2/RGO composite with the mass ratio of SnO_2 to RGO up to 76.1:23.9

3.6. CV behaviors of the composite

Fig. 6a shows the CV curves of the SnO_2/RGO composite with the mass ratio of 76.1:23.9 (SnO_2:RGO), graphene and pure SnO_2 at the sweep rate of 5 mVs^{-1}. It could be found that the area surrounded by CV curves for SnO_2/RGO composite electrode is apparently larger than that of the graphene and pure SnO_2 electrodes at the same scan rate, implying the higher specific capacitance of SnO_2/RGO composite electrode. This result indicates that the electrochemical utilization of SnO_2 has been greatly improved by the introduction of RGO. Additionally, the composite with the mass ratio of 76.1:23.9 (SnO_2:RGO) present the typical box like curve, expected for an ideal capacitor. In order to inspect the capacitive characteristics of the SnO_2/RGO, CV curves of the composite with the mass ratio up to 76.1:23.9 (SnO_2:RGO) at different scan rate were recorded in 1 M H_2SO_4 electrolyte as shown in Fig. 6b. As can be seen from Fig. 6b, no obvious peaks were observed at all scan rates, indicating that the electrodes were charged and discharged at a pseudo-constant rate over the entire voltage cycle. Besides, No obvious distortion in the CV curves is observed as the potential scan rate is increased, even at a high scan rate of 20 mVs^{-1}, the CV curve still retain the rectangular shape. The excellent CV shape at such a high scan rate reveals a very rapid current response on voltage reversal at each end potential. Most importantly, a large magnitude of current response in cyclic voltammetry can not only be attributed to the double-layer processes, but also the highly dispersed SnO_2 nanoparticles onto the RGO sheets might participate in the electrochemical reaction by the following reaction [42]:

$$SnO_2 + H^+ + e^- \leftrightarrow SnOOH \quad (1)$$

This synergism is reasonably attributed to the obvious improvement in the proton diffusion into the nanocomposites during the charge storage/delivery process. In other words, the well-dispersed RGO sheets and mesoporous structure of SnO_2 (see Fig. 3a, f) are helpful to the H^+ ions to diffuse and contact the electroactive surface of composites. Therefore, the capacitive property of the composites should be satisfied.

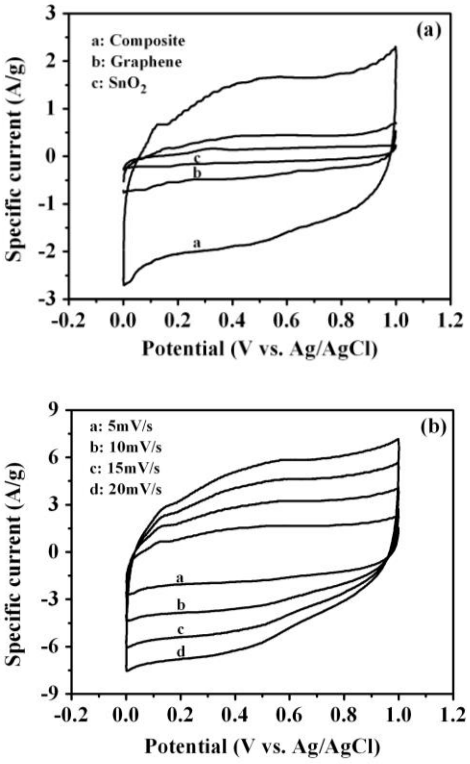

Fig. 6. CV curves of (a) RGO, SnO_2 and the composite with the mass ratio up to 76.1:23.9 (SnO_2:RGO) at the scan rate of 5 $mV\,s^{-1}$ and (b) the composite with the mass ratio up to 76.1:23.9 (SnO_2:RGO) at different scan rates

3.7. Specific capacitance of composites

The applicability of supercapacitors can be directly evaluated by means of the galvanostatic charge-discharge method. The effects of mass ratio on the specific capacitance of composites are given in Fig. 7(a). The high specific capacitance (326 F/g) of the SnO_2/RGO composite with the mass ratio up to 76.1:23.9 (SnO_2:RGO) at a current density of 1 A/g is achieved, which is much higher than the specific capacitance of SnO_2 (30 F/g) and RGO (84 F/g) at the same condition. The remarkable improvement of specific capacitance is probably attributed to the unique structure of composite and the characteristic of reduced graphene oxide. Firstly, a high surface area of SnO_2/RGO composite and additional porosity (see Fig. 3a) can be accessible to the electrolyte into the composite. Secondly, the RGO further improves the conductivity of the composite, which is another factor for obtaining good electrochemical properties. Finally, the significant enhancement in specific capacitance is due to the positive synergistic effect of pseudo-capacitance from SnO_2 and double-layer capacitance from RGO. Moreover, amongst composites, the sample with the optimal mass ratio of 76.1:23.9 (SnO_2:RGO) has the highest specific capacitance, which is attributed to its unique morphology of well-dispersed RGO sheets coated by porous SnO_2 particles. This structure could not only effectively inhibit the stacking/agglomerating of RGO, resulting in high double layer capacitance, but also can exhibit enlarged electrode/electrolyte interface areas, providing high electroactive regions and short diffusion lengths due to the small nanometer-sized and porous SnO_2 particles, which can ensure the high utilization of SnO_2. Fig. 7(b) shows the galvanostatic charge-discharge behavior of the SnO_2/RGO composite as a function of thermal treatment temperature in the potential range between 0.0 and 1.0 V at a specific current of 1 A g^{-1}. As shown in Fig. 7(b), the maximum specific capacitance is reached at heat treatment temperature of 200 °C, indicating that specific capacitance also depends significantly on the treatment temperature and the optimal treatment temperature is 200 °C. The reason is that further thermal treatment for SnO_2/RGO composite results in low electrochemical utilization of composite due to a serious agglomeration of active material. To get more information about the potential of as-synthesized SnO_2/RGO composite with the mass ratio of 76.1:23.9 (SnO_2:RGO) as electrode material for supercapacitor, galvanostatic charge/discharge measurements were carried out in 1 M H_2SO_4 between 0.0 and 1.0 V at various specific current. The charge/discharge curves of the specific capacitance with the specific current are shown in Fig. 7(c). It can be seen that all curves are highly linear and symmetrical at various current densities from 1 to 7 A g^{-1}, which is another typical characteristic of an ideal capacitor. Moreover, even at the high specific current of 7 A g^{-1}, the specific capacitance value is 249 F g^{-1}. This demonstrates the high energy density and stable reversible characteristics of the SnO_2/RGO composite at high currents.

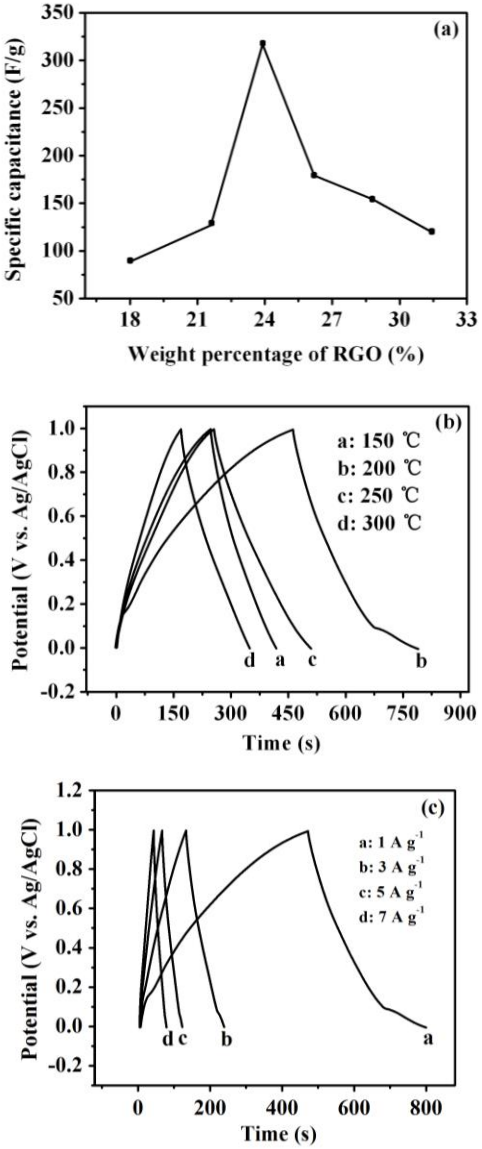

Fig. 7. The specific capacitances of the composites as a function of mass ratios (a), the charge–discharge curves of composites with the mass ratio up to 76.1:23.9 (SnO_2:RGO) at different thermal treatment temperatures (b) and the charge–discharge curves of the composite with the mass ratio up to 76.1:23.9 (SnO_2:RGO) at different specific currents (c)

3.8. EIS analysis of composites

The electrochemical impedance spectroscopy (EIS) analysis has been recognized as one of the principal methods for examining the fundamental behavior of electrode material for a supercapacitor [42]. In our work, EIS measurements were carried out at the bias potential of 0.6 V over the frequency range from 0.1 Hz to 10 kHz. Fig. 8(a) presents the electrochemical impedance spectra in the form of Nyquist plots for SnO_2/RGO composites with different mass ratio, where Z' and Z'' are the real and imaginary parts of the impedance, respectively. As shown in Fig. 8(a), a small semicircle arc and a straight line have been observed for all the composites. The presence of the

small semicircular arc at higher frequencies is attributed to Faradaic reactions. The measured resistance is composed of the following terms: the ionic resistance of electrolyte, the intrinsic resistance of the active material, and the contact resistance (charge transfer resistance) at the active material/current collector interface. Contact resistance can be directly measured as the semicircle diameter [43]. It is noticed that composite with the mass ratio of 76.1:23.9 (SnO_2:RGO) electrode has lower charge transfer resistance (2.1 Ω) than other composite electrode. It showed that the charge transfer between the SnO_2 which well dispersed and grown on the RGO sheets and conductive RGO sheets is a fast process. At low frequencies, the impedance plot for idea electrical double layer capacitors should theoretically be a vertical line, which is parallel to the imaginary axis. From Fig. 8(a), the composite with only mass ratio of 76.1:23.9 (SnO_2:RGO) tends to show purely capacitive feature. Due to the existence of constant phase element [44], the low frequency straight lines of other samples departure from that expected, with a slope angle close to 45°. The slope is attributed to the Warburg resistance resulting from the frequency dependence of ion diffusion and transport in the electrolyte. The large Warburg region of these electrodes indicates the greater variations in ion diffusion path lengths and increased obstruction of ion movement. Fig. 8(b) presents the impedance plots for the composites with mass ratio of 76.1:23.9 (SnO_2:RGO) treated at different temperature. As shown in Fig. 8(b), the impedance behaviors of composites obtained at the thermal treatment temperature of 150, 250 and 300 °C have a deviation from ideal capacitor. For the composites thermally treated at 150 °C, the slope angle at low frequency even smaller than 45°. It indicated that the ions of electrolyte do not penetrate into the particulate and access only the surface of active material. In addition, the equivalent series resistance (ESR) of the electrode can be obtained from the *x* intercept of the Nyquist plot. Composites obtained at the thermal treatment temperature of 150, 200, 250 and 300 °C show comparable ESR at about 2.9, 2.1, 2.4 and 2.6 Ω. This result indicates that charge transfer of composite treated at 200 °C is faster than that of composites treated at other temperatures.

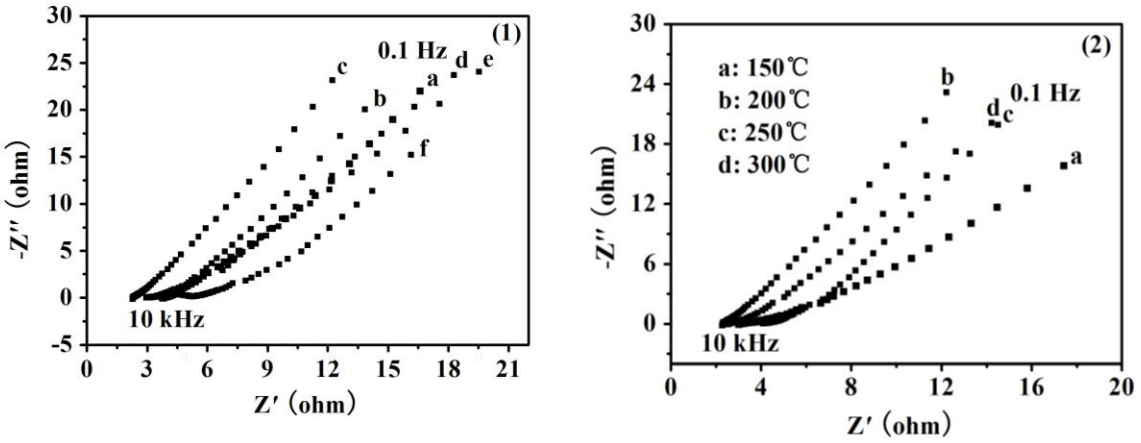

Fig. 8. (1) Nyquist plots of SnO_2/RGO composites with mass ratios of SnO_2 to RGO up to 82:18 (a), 78.4:21.6 (b), 76.1:23.9(c), 73.8:26.2 (d), 71.2:28.8 (e) and 68.5:31.5 (f), and (2) the composites with the mass ratio up to 76.1:23.9 (SnO_2:RGO) thermally treated at different temperatures

3.9. Cycle stability of the composite

The stability and reversibility of an electrode material are important for its use in an electrochemical supercapacitor. Fig. 9 shows the specific capacitance (SC) and coulombic efficiency (η) of the composite with the mass ratio of 76.1:23.9 (SnO_2:RGO) electrode as a function of charge–discharge cycle numbers at a current density of 3 A g^{-1}. From Fig. 9, it can be seen that there is only 2.8% decay in the available capacity over 1000 cycles, which implies an excellent long-term recycling capability. Besides, the specific capacitance increased lightly at initial cycles, and then decreased with continuous cycles. These results indicate that ultrathin flexible RGO sheets can effectively prevent the volume expansion/contraction and aggregation of electroactive materials during the charge/discharge process.

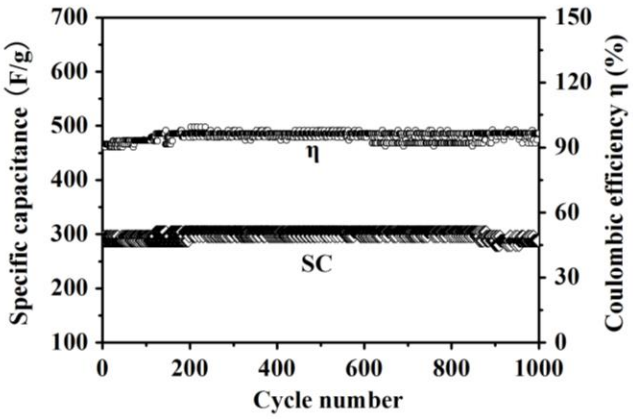

Fig. 9. Life span of the composite with the mass ratio up to 76.1:23.9 (SnO_2:RGO) at 3 A g^{-1}

The coulombic efficiency of the capacitor cell can be calculated from the galvanostatic charge–discharge experiments as follows:

$$\eta\ (\%) = \Delta tC/\Delta tD \times 100 \qquad (2)$$

where ΔtC and ΔtD are the times of charging and discharging with the same current, respectively. The initial coulomb efficiency is 90.1%. However, it increases rapidly with the increment of cycle numbers and almost approaches 96% after 150 cycles, implying that a good reversibility can be obtained after the active materials are activated through electrochemical reactions during charge/discharge processes.

4. Conclusions

SnO_2/RGO composites have be successfully prepared directly starting with GO. The morphology of composite with the mass ratio of 76.1:23.9 (SnO_2:RGO) shows that a great amount of SnO_2 nanoparticles have grown on the RGO sheets. At the same time, as shown in TEM, a large number of RGO exhibits plane morphology due to the appearance of small-sized SnO_2 nanoparticles. Besides, the SnO_2 nanoparticles on the RGO sheets are porous structure, the pores distribute homogeneously through the arrays of SnO_2 nanoparticles on the RGO sheets. This structure can not only increase the distance between the graphene sheets, but also provide rapid diffusion path for SnO_2 participation in electrochemical reaction. Therefore, the composite achieve an extraordinary high specific capacitance of 326 F/g at 1 A g^{-1} in the potential range from 0.0 to 1.0 V, which is much higher as respectively compared with the individual value of the two components. The enhancement in specific capacitance results from positive synergistic effects due to the superimposition of pseudo-capacitance and double-layer capacitance. Moreover, there was only 2.8% decay in the available capacity over 1000 cycles at the current density of 3 A g^{-1}, suggesting that SnO_2/RGO composites are a promising electrode material for supercapacitors.

Acknowledgment

We gratefully acknowledge the financial support offered by the National Natural Science Foundation of China (20963009), Gansu Science and Technology Committee (0803RJA005) and the postgraduate advisor program of Provincial Education Department of Gansu.

References

[1] Y. Chen, X. Zhang, D. C. Zhang, P. Yu, Y. W. Ma, Carbon **49**(2), 573 (2011).
[2] S. K. Mondal, N. Munichandraiah, J. Power Sources **175**(1), 657 (2008).
[3] A. A. F. Grupioni, E. Arashiro, T. A. F. Lassali, Electrochimica Acta **48**(4), 407 (2002).
[4] A. Devadas, S. Baranton, T. W. Napporn, C. Coutanceau, J. Power Sources **196**(8), 4044 (2011).
[5] K. R. Prasad, K. Koga, N. Miura, Chem. Mater **16**(8), 1845 (2004).
[6] Sumanta Sahoo, Jae-Jin Shim, Chem. Eng. **5** (1), 241 (2017).
[7] Xiaoning Tian, Xiaolong Sun, Zhongqing Jiang, Zhong-Jie Jiang, Xiaogang Hao, Dadong Shao, T. Maiyalagan, Appl. Energy Mater. **1**(1), 143 (2018).
[8] Yongmin He, Wanjun Chen, Xiaodong Li, Zhenxing Zhang, Jiecai Fu, Changhui Zhao, Erqing Xie, ACS Nano **7** (1), 174 (2013).
[9] Yongchuan Liu, Xiaofei Miao, Jianhui Fang, Xiangxin Zhang, Sujing Chen, Wei Li, Wendou Feng, Yuanqiang Chen, Wei Wang, Yining Zhang. Appl. Mater. Interfaces **8**(8), 5251 (2016).
[10] Gaind P. Pandey, Tao Liu, Emery Brown, Yiqun Yang, Yonghui Li, Xiuzhi Susan Sun, Yueping Fang, Jun Li, Appl. Mater. Interfaces **8**(14), 9200 (2016).
[11] Yu Ouyang, Xifeng Xia, Haitao Ye, Liang Wang, Xinyan Jiao, Wu Lei, Qingli Hao, Appl. Mater. Interfaces **10**(4), 3549 (2018).
[12] Haidong Bian, Yayuan Tian, Chris Lee, Muk-Fung Yuen, Appl. Mater. Interfaces **8**(42), 28862 (2016).
[13] Mingxi Chen, Huan Wang, Lingzhi Li, Zhe Zhang, Cong Wang, Yu Liu, Wei Wang, Appl. Mater. Interfaces **6**(16), 14327 (2014).
[14] N. L. Wu, Mater. Chem. Phys. **75**(1), 6 (2002).
[15] K. R. Prasad, N. Miura, Electrochem. Commun. **6**(8), 849 (2004).
[16] R. K. Selvan, I. Perelshtein, N. Perkas, A. Gedanken, J. Phys. Chem. C **112**(50), 1825 (2008).
[17] A. Leela Mohana Reddy, S. Ramaprabhu, J. Phys. Chem. C **111**(21), 7727 (2007).
[18] H. W. Wang, Z. A. Hu, Y. Q. Chang, Y. L. Chen, Z. Q. Lei, Z. Y. Zhang, Y. Y. Yang, Electrochim Acta **55**(28), 8974 (2010).
[19] Z. S. Wu, D. W. Wang, W. Ren, J. Zhao, G. Zhou, F. Li, H. M. Cheng, Adv. Funct. Mater. **20**(28), 3595 (2010).
[20] Z. S. Wu, W. Ren, D. W. Wang, F. Li, B. Liu, H. M. Cheng, ACS Nano **4**(10), 5835 (2010).
[21] S. Chen, J. Zhu, X. Wu, Q. Han, X. Wang, ACS Nano **4**(5), 2822 (2010).
[22] S. Chen, J. Zhu, X. Wang, J. Phys. Chem. C **114**(5), 11829 (2010).
[23] H. L. Wang, H. S. Casalongue, Y. Y. Liang, H. J. Dai, J. Am. Chem. Soc. **132**(21), 7472 (2010).
[24] T. Lu, Y. P. Zhang, H. B. Li, L. K. Pan, Y. L. Li, Z. Sun, Electrochimica Acta **55**(13), 4170 (2010).
[25] S. M. Paek, E. J. Yoo, I. Honma, Nano Lett. **9**(13), 72 (2009).
[26] J. Yao, X. P. Shen, B. Wang, H. K. Liu, G. X. Wang, Electrochem. Commun. **11** (10), 1849 (2009).
[27] Y. L. Chen, Z. A. Hu, Y. Q. Chang, H. W. Wang, Z. Y. Zhang, Y. Y. Yang, H. Y. Wu, J. Phys. Chem. C **115**(5), 2563 (2011).
[28] W. S. Hummers, R. E. Offeman, J. Am. Chem. Soc. **80**(6), 1339 (1958).
[29] Z. S. Wu, W. C. Ren, L. B. Gao, J. P. Zhao, Z. P.

Chen, B. L. Liu, D. M. Tang, B. Yu, C. B. Jiang, H. M. Cheng, ACS Nano. **3**(2), 411 (2009).
[30] G X. Wang, X. P. Shen, J. Yao, J. Park, Carbon **47**(8), 2049 (2009).
[31] C. Xu, X. Wang, J. Zhu, X. Yang, L. J. Lu, Mater. Chem. **18**, 5625 (2008).
[32] N. Kovtyukhova, E. Buzaneva, A. Senkevich, Carbon **36**(5-6), 549 (1998).
[33] X. Du, P. Guo, H. H. Song, X. H. Chen, Electrochimica Acta **55**(16), 4812 (2010).
[34] J. F. Scott, J. Chem. Phys. **53**(2), 852 (1970).
[35] J. G. Traylor, H. G. Smith, R. M. Nicklow, M. K. Wilkinson, Phys. Rev. B **3** (10), 3457 (1971).
[36] Q. Dong, H. L. Su, D. Zhang, W. Cao, N. Wang, Langmuir **23**(15), 8108 (2007).
[37] J. X. Zhou, M. S. Zhang, J. M. Hong, Z. Yin, Solid State Communications **138**(5), 242 (2006).
[38] L. Abello, B. Bochu, A. Gaskov, S. Koudryavtseva, G. Lucazeau, M. Roumvantesva, J. Solid State Chem. **135**(1), 78 (1998).
[39] F. H. Aragon, J. A. H. Coaquira, P. Hidalgo, S. W. Silva, S. L. M. Brito, D. Gouveac, P. C. Moraisa, J. Raman Spectrosc. **42**(5), 1081 (2011).
[40] W. C. Zhou, R. B. Liu, Q. Wan, Q. L. Zhang, A. L. Pan, L. Guo, B. S. Zou, J. Phys. Chem. C **113**(1), 1719 (2009).
[41] G. X. Wang, J. Yang, J. Park, X. L. Gou, B. Wang, H. Liu, J. Yao, J. Phys. Chem. C **112**(1), 8192 (2008).
[42] F. H. Li, J. F. Song, H. F. Yang, S. Y. Gan, Q. X. Zhang, D. X. Han, A. Ivaska, L. Niu, Nanotechnology **20**(45), 455602 (2009).
[43] H. L. Guo, X. F. Wang, Q. Y. Qian, F. B. Wang, X. H. Xia, ACS Nano. **3**(9), 2653 (2009).
[44] G. J. Brug, A. V. Eeden, M. Sluyters-Rehbach, J. H. Sluyters, J. Electroanal. Chem. **176**(1-2), 275 (1984).

*Corresponding author: 416665366@qq.com